Arch. Mech., **68**, 4, pp. 309–326, Warszawa 2016

Mixed-mode thermal fracture of AISI 304 stainless steel with temperature-dependent material properties

M. RAJABI, N. SOLTANI

Department of Mechanical Engineering
College of Engineering
University of Tehran
North Karegar Ave.
Jalal Ale Ahmad Blvd.,Tehran, Iran
e-mail: mohammad.rajabi@ut.ac.ir

Mixed-mode thermal fracture of cracked AISI 304 austenitic stainless steel layers under severe thermal gradients of cryogenic and elevated temperatures is studied. Taking into account the variation of thermo-mechanical properties with temperature, the J_k-integral method, incorporating temperature-dependent material properties, is used to determine mixed-mode stress intensity factors from the results of finite element (FE) analysis. Effects of the convection heat transfer coefficient and the temperature of the contacting fluid on the mixed-mode fracture of the steel layers are investigated and it is shown that the mixed-mode stress intensity factors increase nonlinearly with these parameters. Results indicate that for accurate determination of crack tip fracture parameters when severe thermal gradients are present in the material, it is necessary to consider the variation of thermo-mechanical properties with temperature.

Key words: temperature-dependent material properties, stress intensity factor, thermal fracture, cryogenic temperature, AISI 304 austenitic stainless steel.

1. Introduction

Austenitic stainless steels, due to their superior formability and weldability properties, are among the most commonly used and known types of stainless steels. They are used in a wide range of operating temperature conditions, i.e., from cryogenic temperatures of liquid gas tanks to the red-hot temperatures of furnaces and jet engines [1]. For example, when referring to specialty steel industry of the United States [2], it can be seen that the AISI 304 stainless steel type with extraordinary fracture and corrosion resistance behavior is commonly used in a wide range of temperature variations for sever thermal conditions such as very low or very high temperatures. This type of austenitic stainless steel is used in the liquid natural gas (LNG) transport and storage, and for other liquid gas barriers, fuel tanks and cryogenic vessels [3–5]. An explosion or an accidental impact may expose these structures to severe thermal loads caused by elevated and cryogenic temperature. Furthermore, critical components of liquid-propellant engine of aerospace vehicles may encounter thermal cycles between elevated and cryogenic temperatures [6]. The presence of thermal stresses and the existence of defects or cracks in these structures can lead to disastrous consequences [7]. Further thermal and mechanical loads may lead to crack propagation, and, finally, leakage or failure of the structure [8]. Precise analysis and prediction of the life of cracked structures in aerospace and other industries can prevent loss of human lives and reduce the high costs associated with maintenance and/or replacement of components working in such severe conditions.

The thermal fracture problem has been of interest to many researchers. The weight function method was used to compute thermal stress intensity factors in homogeneous [9] and functionally graded hollow cylinders [10, 11] with circumferential cracks. Analytical solutions based on the singular integral equations and numerical calculations using the enriched finite element method were presented in [12] to study the mixed-mode thermo-mechanical fracture of orthotropic functionally graded materials. A finite element discretized symplectic method was developed by Zhou *et al.* [13] for calculation of mixed mode thermal stress intensity factors under steady-state thermal loadings. Recently, Li and Lee [14] have considered the effect of thermal conductivity of air in a penny-shaped crack interior in an elastic solid with uniform steady heat flux on mixed-mode thermal stress intensity factors. A Hankel transform was used to transform the problem to a system of dual integral equations. In most of the studies concerning the problem of a cracked structure subjected to thermal gradients, the variation of material properties with temperature is not considered. In many engineering materials including austenitic stainless steels, thermal and mechanical properties vary with temperature. Thus, when dealing with high thermal gradients in a structure, it is necessary to include the effects of temperature on the variation of material properties. This is discussed by Chan *et al.* [15] in a report on modeling and analysis of isotropic materials for harsh environment. Several other researchers have also considered the effects of temperature-dependent material properties on the thermal behavior of engineering structures. Noda [16] discussed the effect of temperature-dependent material properties on stress fields in plates, and found that consideration of temperature dependency of material properties has a significant effect on the magnitude and distribution of stress fields. Otto *et al.* [17] investigated the influence of temperature on mechanical properties of a high entropy alloy (e.g., AISI 304 family) at low and elevated temperatures, and they have shown that temperature has considerable effect on tensile properties of this kind of materials. On the other hand, in many cases the existence of thermal gradient in the structure is due to the contact of the solid material with some cooling or heating fluid. Thus, for a precise estimation of surface temperatures in pressurized vessels and structures that transfer heat to the surrounding fluids, the effect of convection heat transfer with the contacting fluid should be taken into account [18, 19]. In this study, the effects of temperature-dependent material properties on the mixed-mode thermal fracture of cracked austenitic stainless steels that are subjected to convective thermal boundary conditions are investigated. A J_k-integral method incorporating temperature dependency of material properties is used to calculate mixed-mode stress intensity factors from the results of finite element analysis. Mixed mode stress intensity factors are obtained for the two cases of temperature-dependent and temperature-independent material properties, and the results are compared for these two cases. The effects of convection heat transfer coefficient and the fluid temperature on the mixed-mode fracture parameters are also studied.

2. Formulation

2.1. J_k-integral

J_k-integral is defined over a vanishingly small curve at a crack tip. Mixed-mode stress intensity factors can be evaluated using the components of this line integral. Referring to Dag [20], the expression for J_k-integral can be expressed as

$$J_k = \int\limits_{\gamma_0 \to 0} (W n_k - \sigma_{ij} n_j u_{i,k})\, ds, \tag{2.1}$$

where $i, j, k = 1, 2$, W represents the internal strain energy density, n_k is the component of the normal vector to the vanishing curve γ_0 which encompasses a crack tip, σ_{ij} is the stress component and u_i denotes the displacement component (see Fig. 1). Plane stress/strain conditions are assumed in Eq. (2.1) and $u_{.,k}$ represents differentiation with respect to kth coordinate. It should be noted that J_1 represents the energy release rate (J-integral) that was introduced by Rice [21]. For an isotropic material with temperature-dependent thermal and mechanical properties the elastic stress-strain relations are given by:

$$\sigma_{ij} = 2\mu\varepsilon_{ij} + \left[\lambda\varepsilon_{kk} - (3\lambda + 2\mu)\int\limits_{T^*}^{T} \alpha(\xi)\, d\xi\right]\delta_{ij}, \tag{2.2}$$

where μ and λ are Lamé constants which depend on temperature and α is the coefficient of thermal expansion which is also taken to be dependent on temperature. T is the temperature at any point and T^* is the reference stress-free temperature, and δ_{ij} denotes the Kronecker delta. In addition, the strain energy density is given by:

$$W = \frac{1}{2}\sigma_{ij}\left(\varepsilon_{ij} - \int\limits_{T^*}^{T} \alpha(\xi)\, d\xi \delta_{ij}\right). \tag{2.3}$$

In this study, it is assumed that a generic material property of the constituent materials is dependent on the temperature as

$$P = P(T), \tag{2.4}$$

where P is any material property (except Poisson's ratio which is taken to be constant in this study). This function can be achieved by using experimental data in variation of material properties with temperature. Substituting Eq. (2.2) into Eq. (2.3) and using Eq. (2.4), it is possible to write:

$$W = W(\varepsilon_{ij}, \mu, \lambda, \psi), \tag{2.5}$$

where ψ is defined as

$$\psi = \psi(T) = \int_{T^*}^{T} \alpha(\xi)\, d\xi. \tag{2.6}$$

It should be noted that for the case of plane strain considered in this study, the dependency of elastic strain energy density is only upon the in-plane components of the symmetric strain tensor (i.e., ε_{11}, ε_{22}, ε_{12}). Following the procedure given by Dag [20], for a crack with traction-free surfaces the J_k-integral defined by Eq. (2.1) on a vanishing small contour at a crack tip can be converted to a combination of area and line integrals and is given by:

$$J_1 = \iint\limits_{A} (\sigma_{ij}u_{i,1} - W\delta_{1j})q_{,j}\, dA - \iint\limits_{A} (W_{,1})_{\varepsilon xpl} q\, dA, \tag{2.7}$$

$$\begin{aligned} J_2 = {} & \iint\limits_{A} (\sigma_{ij}u_{i,2} - W\delta_{2j})q_{,j}\, dA - \iint\limits_{A} (W_{,2})_{\varepsilon xpl} q\, dA \\ & - \int\limits_{\gamma_S} (W^{+} - W^{-})q\, ds \qquad (i, j = 1, 2). \end{aligned} \tag{2.8}$$

Area A and the contours γ_s^{+} and γ_s^{-} are shown in Fig. 1.

Additionally, W^{-} and W^{+} represent strain energy densities evaluated on the lower and upper crack faces, respectively. Smooth function "q" for a circular path around the crack tip can be expressed as [20]

$$q(x_1, x_2) = 1 - \frac{\sqrt{x_1^2 + x_2^2}}{R}. \tag{2.9}$$

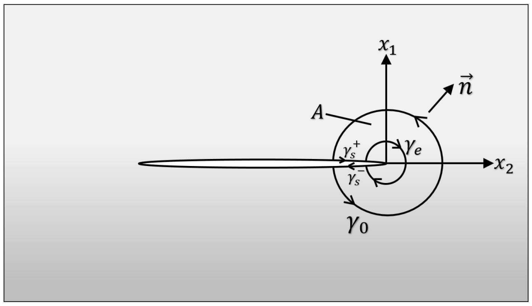

Fig. 1. Domain and paths of integration in the crack tip region.

The expression for $(W_{,k})_{expl}$ in Eqs. (2.7) and (2.8) is given by:

$$(W_{,k})_{expl} = \frac{\partial W}{\partial \mu}\left(\frac{\partial \mu}{\partial T}\frac{\partial T}{\partial x_k}\right) + \frac{\partial W}{\partial \lambda}\left(\frac{\partial \lambda}{\partial T}\frac{\partial T}{\partial x_k}\right) + \frac{\partial W}{\partial \psi}\left(\frac{\partial \psi}{\partial T}\frac{\partial T}{\partial x_k}\right). \tag{2.10}$$

Terms $\partial\mu/\partial T$, $\partial\lambda/\partial T$ and $\partial\psi/\partial T$ can be computed using Eq. (2.4). Other terms in Eq. (2.10) can be calculated numerically during the finite element computations by using the corresponding shape functions of the elements. Further details on the FE implementation and numerical procedure can be found in [20].

2.2. Mixed-mode stress intensity factors calculation

From the calculated J_1 and J_2, the following relations can be used for calculation of K_I and K_{II}, [20]:

$$J_1 = \frac{K_I^2 + K_{II}^2}{E'_{tip}}, \qquad J_2 = -\frac{2K_I K_{II}}{E'_{tip}}, \tag{2.11}$$

where $E'_{tip} = E_{tip}/(1-\nu_{tip}^2)$ for plane strain in which E_{tip} and ν_{tip} denote elasticity modulus and Poisson's ratio at the crack tip. To determine the correct signs of the stress intensity factors from the J_k-integral values from Eq. (2.11), one may refer to the method presented by Dag [20], in which the J_2 expression is calculated for two different choices of the γ_s line.

3. AISI 304 temperature dependent material properties (TDMP)

Chemical composition of AISI 304 typical stainless steel is reported by Kirillov [22] and presented in Table 1. To determine the coefficients of Eq. (2.4) for a generic material property $P(T)$, the experimental data available in the literature on material properties of typical austenitic stainless steel AISI 304 as a function of temperature for cryogenic and elevated temperatures are used.

Table 1. Chemical composition of AISI 304 typical stainless steel [22].

Element concentration (%)						
C	Cr	Ni	Ti	Nb	Mo	W
< 0.08	18	10	< 0.05	< 0.05	< 0.05	< 0.05

Based on experimental data for below room temperature of liquid nitrogen temperature (77°K) material properties of typical AISI 304 stainless steel [23–25] and also its elevated temperature material properties [26, 27], temperature-dependent function $P(T)$ for modulus of elasticity $E(T)$, coefficient of thermal expansion $\alpha(T)$ and thermal conductivity $k(T)$ are constructed. Based on experimental data that is shown in Fig. 2, the function $E(T)$ (GPa) can be expressed as follows:

$$E(T) = -2 \times 10^{-8} T^3 + 10^{-5} T^2 - 0.0686 T + 215.05. \tag{3.1}$$

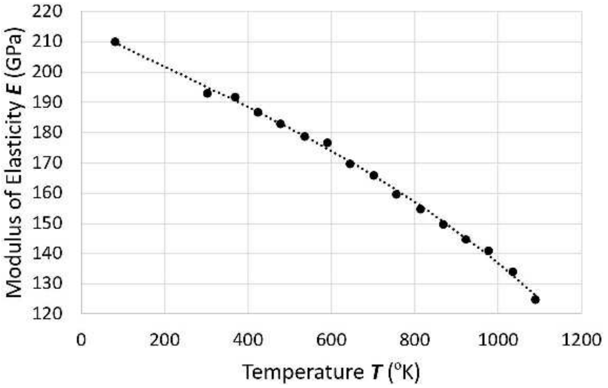

Fig. 2. Modulus of elasticity of AISI 304 stainless steel as a function of temperature; points: experimental data [23–27], dot-line: Eq. (3.1).

Using the experimental data shown in Fig. 3, the coefficient of thermal expansion (1/°K) can be expressed as

$$\alpha(T) = 10^{-8} T + 10^{-5}. \tag{3.2}$$

Coefficients of Eq. (2.4), for the thermal conductivity (W/m°K), can also be determined using the experimental data shown in Fig. 4, as follows:

$$k(T) = 4 \times 10^{-8} T^3 - 7 \times 10^{-5} T^2 + 0.0547 T + 3.9525. \tag{3.3}$$

Due to the lack of experimental data, the Poisson's ratio is taken as constant with temperature, and equal to $\nu = 0.3$.

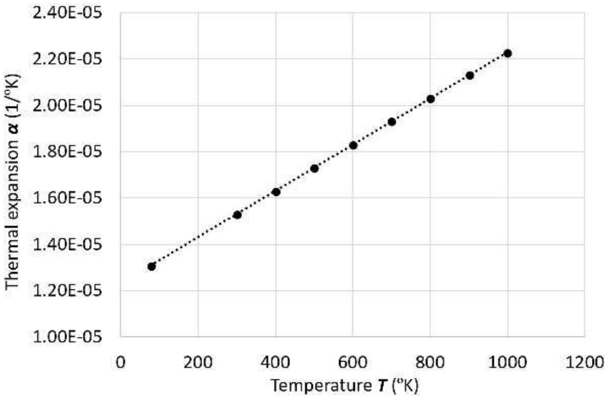

Fig. 3. Coefficient of thermal expansion of AISI 304 stainless steels as a function of temperature; points: experimental data [23–27], dot-line: Eq. (3.2).

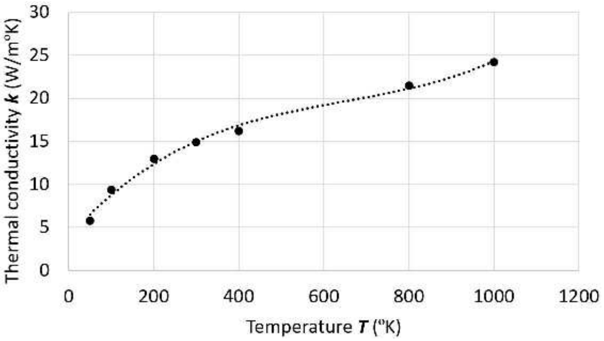

Fig. 4. Thermal conductivity of a typical 304 stainless steel as a function of temperature; points: experimental data [23–27], dot-line: Eq. (3.3).

4. Finite element modeling and computation

A cracked layer made of AISI 304 austenitic stainless steel that is subjected to thermal boundary conditions at its lower and upper surfaces is shown in Fig. 5. As shown in this figure, the layer has a width of $2W$ and its lower surface at $y = -h_2$ is subjected to constant prescribed temperature of T_0. Convective heat transfer and thermal boundary conditions prevail at upper surface of the layer at $y = h_1$. The temperature of the fluid that is in contact with the upper surface is T_∞ and the convection heat transfer coefficient between the layer and the fluid is denoted by h_c. An embedded crack of length $2a$ is located at $y = 0$ and is aligned parallel to the boundaries.

To determine the nodal temperatures and displacement field, a finite element model of the layer is constructed and analyzed using the ABAQUS commercial

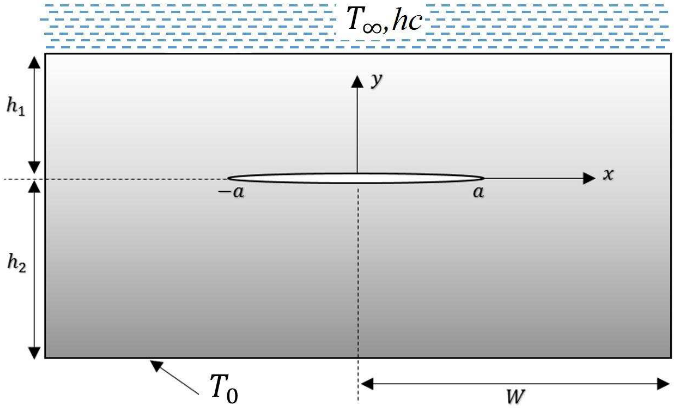

Fig. 5. Geometry of the AISI 304 stainless steel layer.

software. To include changes of material properties with temperature, variations of thermal and mechanical properties of the layer with temperature are implemented using the user subroutines UMAT and UMATHT. Based on the definition of the J_k-integral in Eqs. (2.7) and (2.8), a post-processing routine is also developed to compute the values of energy integrals and the corresponding mixed-mode stress intensity factors from the results of the FE analysis, this procedure is schematically shown in Fig. 6. Due to symmetry, only a half of the layer is modeled and analyzed. Region $0 < x < W$ is considered for the calculation of crack tip fracture parameters at $x = a$. For $x = -a$, mixed-mode stress intensity factors (SIFs) can be calculated by using: $K_I(-a) = K_I(a)$ and $K_{II}(-a) = -K_{II}(a)$. The generated FE model contains 9084 nodes and 3023 elements.

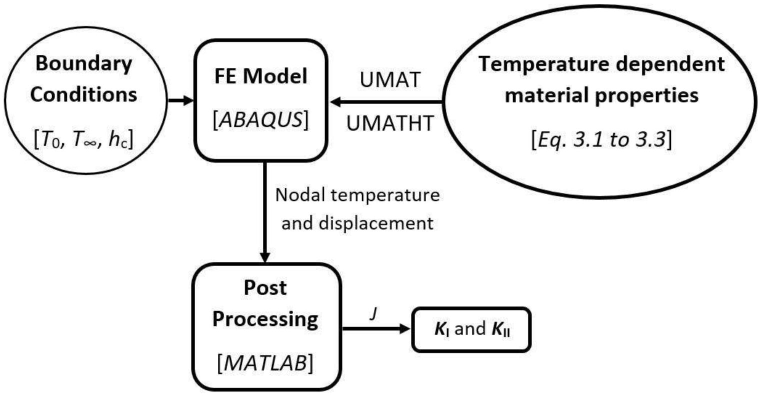

Fig. 6. Calculation procedure of stress intensity factors.

To obtain steady-state temperature distribution in the FE model, the following nonlinear differential equation for two-dimensional governing heat transfer equation can be used:

$$\frac{\partial}{\partial x}\left(k(T)\frac{\partial T}{\partial x}\right)+\frac{\partial}{\partial y}\left(k(T)\frac{\partial T}{\partial y}\right)=0, \tag{4.1}$$

where k is the conductivity coefficient defined in Eq. (3.3), which is dependent on temperature. The above equation should be solved considering the following boundary conditions:

$$k(T)\frac{\partial T}{\partial x}\bigg|_{(\pm W,y)}=0, \tag{4.2}$$

$$k(T)\frac{\partial T}{\partial y}\bigg|_{([-a,a],\pm 0)}=0, \tag{4.3}$$

$$k(T)\frac{\partial T}{\partial y}\bigg|_{(x,h_1)}=h_c[T_\infty-T(x,h_1)], \tag{4.4}$$

$$T(x,-h_2)=T_0. \tag{4.5}$$

Equation (4.2) represents adiabatic surfaces at $x=\pm W$ and Eq. (4.3) states that the crack faces are also considered to be isolated. Equations (4.4) and (4.5) state the prescribed thermal boundary conditions on the upper and lower surface of the layer as mentioned before. In this study, the temperature distribution is determined by implementing the temperature-dependent conductivity coefficient in the FE model by using the user subroutine UMATHT. The temperature distribution is then calculated by performing a heat transfer analysis in the FE environment with 2975 quadratic quadrilateral elements of type DC2D8 plus 48 quadratic triangular elements of type DC2D6 at the crack tip in peripheral direction.

Displacement field is determined by implementing temperature-dependent material properties in the FE model using the user subroutine UMAT and performing static analysis with full integration options of used elements with 2975 quadratic quadrilateral elements of type CPE8R and 48 quadratic triangular elements of type CPE6M around the crack tip in peripheral direction. In Fig. 7, the steady-state temperature distribution in the deformed configuration of the FE model for $T_0 = 77^\circ$K, $T_\infty = 1000^\circ$K and $h_c = 5$ W/m$^{2\circ}$K is shown. Note that since the crack faces are adiabatic, temperature distributions along upper and lower crack faces are not the same.

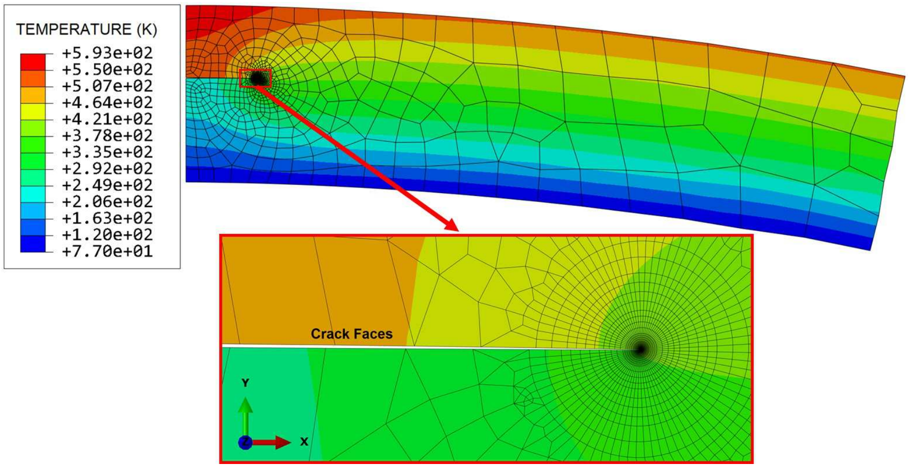

Fig. 7. Temperature distribution and element configuration in a deformed generated FE model ($T_0 = 77°\mathrm{K}$, $T_\infty = 1000°\mathrm{K}$ and $h_c = 5\ \mathrm{W/m^2\ °K}$).

5. Numerical results

In this section, the numerical results of mixed-mode thermal stress intensity factors for the AISI 304 austenitic stainless steel layer (Fig. 5) with temperature-dependent thermal and mechanical properties are presented. The layer is initially assumed to be at the reference temperature of $T^* = 27°\mathrm{C}$ (300°K). Lower side of the specimen is then cooled down to cryogenic temperature of liquid nitrogen, $T_0 = -196°\mathrm{C}$ (77°K). This temperature can be reached by exposing the lower surface of the specimen to liquid nitrogen. As mentioned before, the upper surface of the layer at $y = h_1$ is assumed to be in contact with a fluid of bulk temperature T_∞, which is assumed to take different values from $-73°\mathrm{C}$ (200°K) to 727°C (1000°K). The convection heat transfer coefficient, h_c, is also varied from $0.5\ \mathrm{W/m^2\ °K}$ (almost insulating surface) to infinity (conducting surface) to investigate its effect on the mixed-mode fracture parameters. All other surfaces, including crack faces, are considered to be insulated which leads to a two-dimensional temperature field near the crack faces. Dependency of material properties on temperature is considered using Eqs. (3.1)–(3.3).

Because of the symmetry, only half of the model shown in Fig. 5 is simulated and analyzed in the FE analyses. In this study, the region $0 < x < W$ with $a = 1$, $W = 10a$, $h_1 = a$, and $h_2 = 1.5a$ is considered and modeled for the calculation of crack tip parameters at $x = a$.

To investigate the influence of variation of material properties with temperature on steady-state temperature distribution across crack surfaces, material properties are once considered to be temperature independent and then dependent on temperature. Figure 8 illustrates the steady-state temperature distribution across crack surfaces for various values of the heat transfer coefficient h_c of a fluid with bulk temperature of $T_\infty = 1000°\mathrm{K}$ in the two states of temperature dependent material properties (TDMP) and temperature independent material properties (TIMP).

Material properties in the temperature-independent state are set to P (300°K) by using Eqs. (3.1)–(3.3). Since no heat flow is assumed on the crack faces, the temperatures of the upper and lower crack surfaces are not equal. $T(x, 0^+)$ represents the temperatures of the upper crack surface and a point on this surface has a larger temperature than the temperature of a corresponding point on the lower crack surface, which is indicated by $T(x, 0^-)$. These two temperature profiles merge at $x \to a$. It can be seen that in the state of TDMP, for

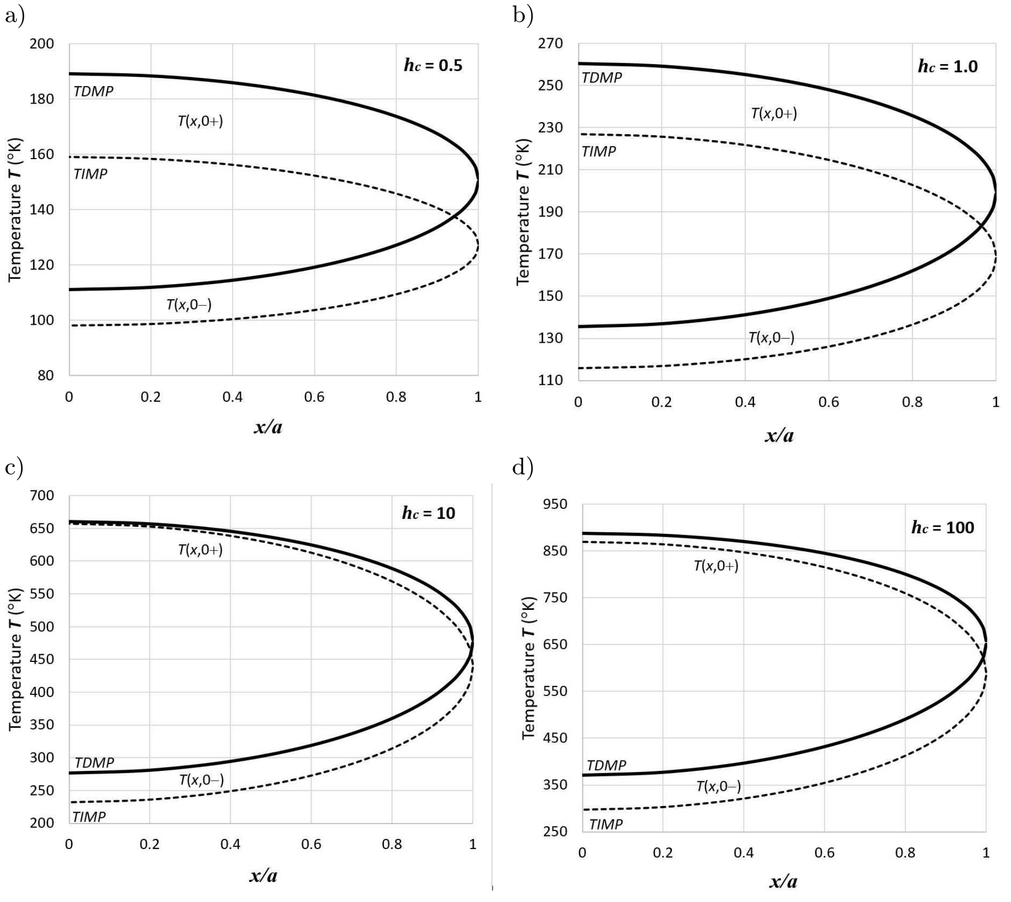

Fig. 8. Steady-state temperature profiles across crack surfaces for various amounts of h_c in two states of TDMP and TIMP, $T_\infty = 1000°\mathrm{K}$ and $T_0 = 77°\mathrm{K}$.

all values of h_c, temperature values are higher than their corresponding values in the state of TIMP.

Furthermore, as the value of h_c decreases, difference between temperature profiles of crack surfaces in the two states of TDMP and TIMP increases. This can be explained by considering that the crack surfaces are assumed to be isolated, which intensifies the effect of input heat flux on the upper crack face.

In Fig. 9, temperature profiles of upper and lower crack surfaces for various values of h_c in the state of TDMP are shown. The effect of convective heat transfer coefficient of a fluid with bulk temperature of $T_\infty = 1000°\text{K}$ on temperature profiles of crack faces can be investigated from this figure. As the h_c increases, all temperature values in both upper and lower faces increase, and this increase is bounded by a maximum value when $h_c \to \infty$. Also it can be concluded that the effect of h_c on temperature profiles is nonlinear.

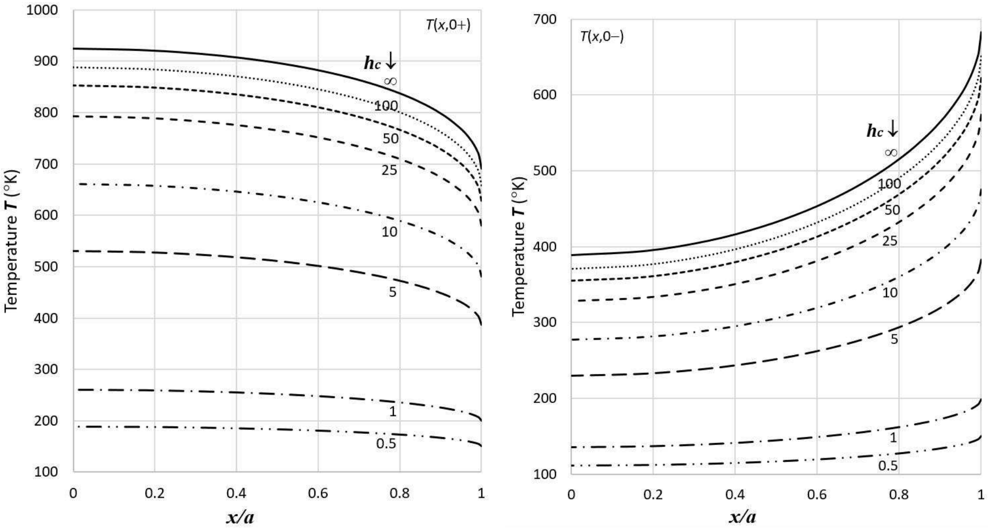

Fig. 9. Temperature profiles of upper and lower crack surfaces for various amounts of h_c in the state of TDMP, $T_\infty = 1000°\text{K}$ and $T_0 = 77°\text{K}$.

In order to verify our results for stress intensity factor computation, the problem of an edge cracked specimen as described in [28] is considered here. The geometry of the problem is shown in Fig. 10. A single-edge-cracked specimen is subjected to a convection heat transfer at its edges, and the mode I stress intensity factor values are to be evaluated under this thermal boundary conditions. In this example, $h_1 = 2$, $h_2 = 2$, $W = 1$, $a = 0.1 \sim 0.8$, $T_0 = 273.15°\text{K}$ (0°C) and $T_2 = 274.15°\text{K}$ (1°C), $E = 1.0 \times 10^5$ Pa, $v = 0.3$, $\alpha = 1.67 \times 10^{-5}\,°\text{C}^{-1}$ and the material properties are assumed to be temperature-independent.

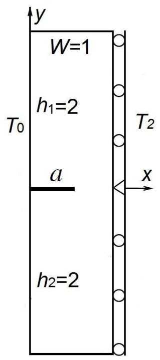

Fig. 10. Geometry of the problem reported in [28].

In Table 2, a comparison between the results reported in [28] and those computed in this study using the present method are shown. A good agreement between the results of the two studies is observed.

Table 2. Mode I stress intensity factor computed by the FEA [28] and the current study.

a/W	K_I (Pa·m$^{0.5}$) (plane strain conditions)	
	FEA [28]	J_k integral, (current study)
0.1	0.6454	0.6416
0.2	0.7760	0.7733
0.3	0.7951	0.7980
0.4	0.7527	0.7534
0.5	0.6705	0.6697
0.6	0.5601	0.5611
0.7	0.4288	0.4280
0.8	0.2825	0.2810

Another verification example is considered for TIMP, in which the mixed-mode stress intensity factors of the problem shown in Fig. 5 are directly calculated using ABAQUS built-in formulation for the calculation of stress intensity factors. The results of mixed-mode stress intensity factors directly obtained from the FE analysis are compared to those computed using the J_k integral formulation of the current study in Table 3.

The geometric and thermal properties corresponding to definitions given in Fig. 5 are assumed to be: $h_1 = 1.5$, $h_2 = 1$, $W = 10$ and $a = 1$, $T_0 = 77$°K,

Table 3. Mixed mode stress intensity factors computed with ABAQUS and J_k integral method in current study in the state of TIMP (plane strain conditions).

h_c (W/m^2 °K)	K_I (MPa·m$^{0.5}$)		K_{II} (MPa·m$^{0.5}$)	
	ABAQUS	J_k integral, (current study)	ABAQUS	J_k integral, (current study)
0.5	6.7333	6.7332	44.3876	44.3878
1	12.3037	12.3034	81.1033	81.1034
5	36.0367	36.0356	237.7068	237.7067
10	47.1575	47.1578	311.1011	311.1012
25	57.4033	57.4023	378.5030	378.5032
50	61.6099	61.6062	406.2021	406.2026
100	63.8001	63.8033	421.0111	421.0078

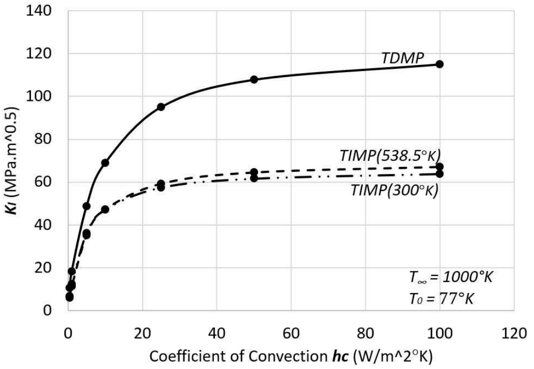

a) Mode I stress intensity factor as a function of h_c

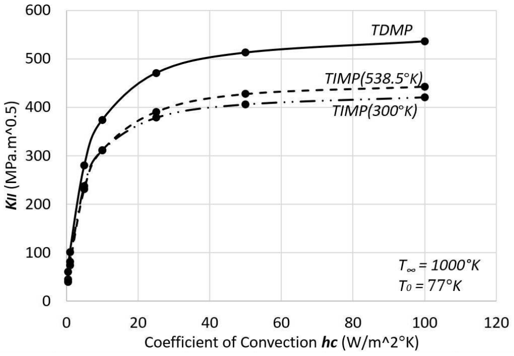

b) Mode II stress intensity factor as a function of h_c

Fig. 11. Thermal mixed mode stress intensity factors as a function of h_c, in the two states of TDMP and TIMP, TIMP (300°K) for material properties at 300°K and TIMP (538.5°K) for material properties at $T_{\mathrm{av}}= 538.5$°K.

$T_\infty = 1000°\text{K}$ and $h_c = 0.5 \sim 100\ \text{W/m}^2\,°\text{K}$. All material properties are set to be constant at P (300°K). Excellent agreement between the results of the current study with those reported by ABAQUS is observed.

The effect of convection heat transfer coefficient h_c on the mixed-mode stress intensity factors is depicted in Fig. 11 in which the bulk fluid temperature is considered to be $T_\infty = 1000°\text{K}$. In those figures, the results are illustrated for two cases for which the material properties are considered to be: (i) dependent on the temperature, and (ii) constant with the temperature.

For the case in which the thermo-mechanical properties are considered to be independent of temperature, the properties are computed at $T = 300°\text{K}$ and $T = T_{\text{av}} = (1000 + 77)/2 = 538.5°\text{K}$ using Eqs. (3.1)–(3.3). The results indicate that temperature dependency of material properties has a considerable effect on the mixed-mode stress intensity factors of the specimen. Comparing mixed-mode stress intensity factors calculated with TIMP at $T = 300°\text{K}$ and

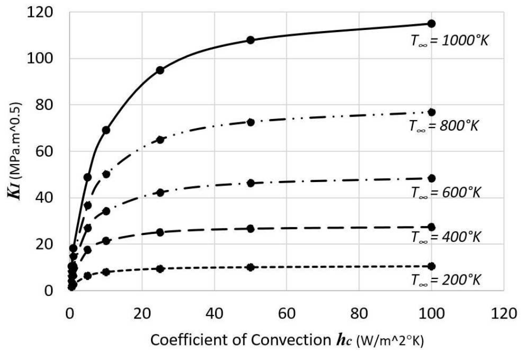

a) Mode I stress intensity factor

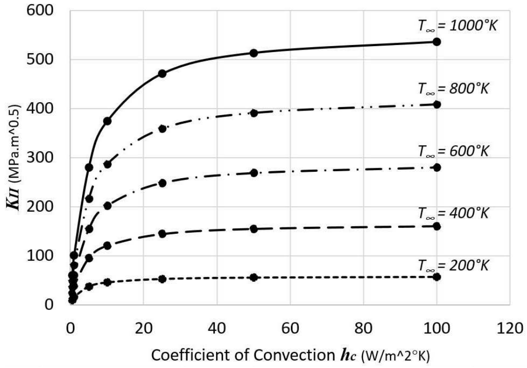

b) Mode II stress intensity factor

FIG. 12. Effect of fluid temperature T_∞ on thermal mixed mode stress intensity factors (in the case of TIMP).

$T_{\text{av}} = 538.5°\text{K}$ reveals no significant change in K_I and K_{II}, which means that it is the temperature dependency of the material properties that affects the values of SIFs when compared to the state of TIMP.

Mixed mode SIFs only change up to 5% in the case of TIMP when we choose to compute the material properties at $T_{\text{av}} = 538.5°\text{K}$ instead of $T = 300°\text{K}$, while by comparing SIFs in the two states of TIMP and TDMP an up to 80% increase in K_I and a 27% increase in K_{II} values are observed. Neglecting variation of material properties with temperature can result in underestimation of stress intensity factors and non-conservative estimations of the fatigue life of the structure. It is also evident that the mixed-mode stress intensity factors monotonically increase with the convection heat transfer coefficient in both considered cases.

Figure 12 indicates the effect of fluid temperature on the mixed-mode thermal stress intensity factors of the layer when the material properties are considered to be dependent on temperature. It is evident that the fluid temperature has an increasing and nonlinear effect on the mixed-mode stress intensity factors and effect of temperature is more pronounced for mode II stress intensity factor.

6. Conclusions

In this study, the effects of TDMP on the mixed-mode fracture of AISI 304 austenitic stainless steel layer subjected to severe thermal gradients of cryogenic and very high temperatures were investigated. Mixed-mode stress intensity factors were calculated by performing the FE simulations and using the results of the FE analysis with the J_k-integral formulation. A suitable form of variation of material properties with temperature was assumed and the coefficients of the resulting expression were determined using the available experimental data. A comparison of crack tip fracture parameters for the two cases of TIMP and TDMP reveals the following results:

- The convective heat transfer coefficient and the bulk temperature of the fluid have considerable effect on the distribution of the temperature in the layer. Mixed-mode crack tip fracture parameters are also strongly dependent on the convective fluid properties.
- Mixed-mode stress intensity factors calculated considering variation of material properties with temperature are higher than the corresponding values evaluated with constant material properties.
- In the state of TIMP, no significant change in mixed-mode SIFs is observed when constant material properties are evaluated at room temperature or T_{av} which is mean value of temperature gradient applied on the layers. Differences between mixed-mode SIFs in these cases is up to 5%, while considering temperature dependency of material properties in formulations, SIFs change up to 80%.

- Differences between crack tip parameters calculated in the two states of TDMP and TIMP become bigger more pronounced when temperature gradient applied on the layer is increased.

Since evaluation of stress intensity factors with constant thermo-mechanical properties of AISI 304 stainless steels result in non-conservative results, it is necessary to include the dependency of material properties on temperature for the design and the fatigue life evaluation of engineering structures that are subjected to extreme thermal gradients such as those operating in cryogenic or high temperature environments.

References

1. M.F. Mcguire, *Stainless Steels for Design Engineers*, ASM International, Ohio, 2008.
2. S.S.I.U.S, S.S.I.N.A, N.D.I., A.I.S.I., *Design Guidelines for the Selection and Use of Stainless Steel*, No. 9014, SSINA, Washington D.C., 1993.
3. A.S. Adamou, *Cryogenic tanks recertification: case study for operational-life extension*, Oil and Gas Facilities, **4**, 88–100, 2015.
4. J.H. Kim, S.K. Kim, M.H. Kim, J.M. Lee, *Numerical model to predict deformation of corrugated austenitic stainless steel sheet under cryogenic temperatures for design of liquefied natural gas insulation system*, Materials & Design, **57**, 26–39, 2014.
5. L.O. Voormeeren, A. Bilim, A.W. Vredeveldt, *Impact resistance of cryogenic bunker fuel tanks*, ASME 33rd International Conference on Ocean, Offshore and Arctic Engineering, ASME, 2014.
6. Z. Guédé, B. Sudret, M. Lemaire, *Life-time reliability based assessment of structures submitted to thermal fatigue*, International Journal of Fatigue, **29**, 1359–1373, 2007.
7. W. Dornowski, *Influence of finite deformations on the growth mechanism of microvoids contained in structural metals*, Archives of Mechanics, **51**, 71–86, 1999.
8. V.M. Mirsalimov, N.M. Kalantarly, *Crack nucleation in circular disk under mixed boundary conditions*, Archives of Mechanics, **67**, 115–136, 2015.
9. S.M. Nabavi, R. Ghajar, *Analysis of thermal stress intensity factors for cracked cylinders using weight function method*, International Journal of Engineering Science, **48**, 1811–1823, 2010.
10. I. Eshraghi, N. Soltani, *Thermal stress intensity factor expressions for functionally graded cylinders with internal circumferential cracks using the weight function method*, Theoretical and Applied Fracture Mechanics, **80**, 170–181, 2015.
11. I. Eshraghi, N. Soltani, M. Rajabi, *Transient stress intensity factors of functionally graded hollow cylinders with internal circumferential cracks*, Latin American Journal of Solids and Structures, an ABCM Journal, **13**, 1738–1762, 2016.
12. S. Dag, Y. Bora, S. Duy Gu, *Mixed-mode fracture analysis of orthotropic functionally graded materials under mechanical and thermal loads*, International Journal of Solids and Structures, **44**, 7816–7840, 2007.

13. Z. ZHOU, A.Y.T. LEUNG, X. XU, X. LUO, *Mixed-mode thermal stress intensity factors from the finite element discretized symplectic method*, International Journal of Solids and Structures, **51**, 3798–3806, 2014.
14. X.F. LI, K.Y. LEE, *Effect of heat conduction of penny-shaped crack interior on thermal stress intensity factors*, International Journal of Heat and Mass Transfer, **91**, 127–134, 2015.
15. K.S. CHAN, U.S. LINDHOLM, S. BODNER, *Constitutive modeling for isotropic materials*, NASA Southwest Research Institute, Texas, 1988.
16. N. NODA, *Thermal stresses in materials with temperature-dependent properties*, Applied Mechanics Reviews, **44**, 383–397, 1991.
17. F. OTTO, A. DLOUHÝ, C. SOMSEN, H. BEI, G. EGGELER, E.P. GEORGE, *The influences of temperature and microstructure on the tensile properties of a CoCrFeMnNi high-entropy alloy*, Acta Materialia, **61**, 5743–5755, 2013.
18. K. CHIDA, *Surface temperature of a flat plate of finite thickness under conjugate laminar forced convection heat transfer condition*, International Journal of Heat and Mass Transfer **43**, 639–642, 2000.
19. N. PARVEEN, M.A. ALIM, *MHD free convection flow with temperature dependent thermal conductivity in presence of heat absorption along a vertical wavy surface*, Procedia Engineering **56**, 68–75, 2013.
20. S. DAG, *Mixed-mode fracture analysis of functionally graded materials under thermal stresses: a new approach using J_k-integral*, Journal of Thermal Stresses **30**, 269–296, 2007.
21. J.R. RICE, *A path independent integral and the approximate analysis of strain concentration by notches and cracks*, Journal of applied mechanics, **35**, 379–386, 1968.
22. P.L. KIRILLOV, *Thermo physical properties of materials for nuclear engineering*, Institute for Heat and Mass Transfer in Nuclear Power Plants, Obninsk, 2006.
23. R.F. BARRON, *Cryogenic Systems*, Clarendon, Oxford, 1985.
24. J.W. EKIN, *Experimental Techniques for Low Temperature Measurements*, Oxford Univ. Press, Oxford, 2006.
25. T.H.K. BARRON, J.G. COLLINS, G.K. WHITE, *Thermal expansion of solids at low temperatures*, Advances in Physics, **29**, 609–730, 1980.
26. L.A. GARDNER, K.T.NG. INSAUSTI, M. ASHRAF, *Elevated temperature material properties of stainless steel alloys*, Journal of Constructional Steel Research **66**, 634–647, 2010.
27. J.N. REDDY, C.D. CHIN, *Thermomechanical analysis of functionally graded cylinders and plates*, Journal of Thermal Stresses, **21**, 593–626, 1998.
28. K.C. AMIT, J.H. KIM, *Interaction integrals for thermal fracture of functionally graded materials*, Engineering Fracture Mechanics, **75**, 2542–2565, 2008.

Received January 10, 2016; revised version June 6, 2016.